Research Network FWF S105

Photoacoustic Imaging in
Medicine and Biology

`http://pai.uibk.ac.at`

A Reconstruction Algorithm for Photoacoustic Imaging based on the Nonuniform FFT

M. Haltmeier, O. Scherzer
and G. Zangerl

August 2008

PAI Report No. 3

Der Wissenschaftsfonds.

universität
innsbruck

A Reconstruction Algorithm for Photoacoustic Imaging based on the Nonuniform FFT

M. Haltmeier[1] O. Scherzer[1,2] G. Zangerl[1]

[1]Department of Mathematics
University of Innsbruck
Technikerstr. 21a
6020 Innsbruck, Austria

[2]Radon Institute of Computational
and Applied Mathematics
Altenberger Str. 69
4040 Linz, Austria

{Markus.Haltmeier,Otmar.Scherzer,Gerhard.Zangerl}@uibk.ac.at

August 27, 2008

Abstract. In this article we are concerned with photoacoustic imaging for the electromagnetic absorption coefficient of a medium from recorded acoustic signals with detectors that are arranged on lines or planes outside of the medium. In the literature Fourier reconstruction algorithms have been proposed, which require interpolation of the sampled acoustic signals on the transducers in the Fourier space domain. As documented in the literature these methods are not very efficient numerically or produce serious artifacts. The proposed algorithm uses the nonuniform fast Fourier transform. As we show below this algorithm can be implemented efficiently and avoids serious artifacts.

Keywords: Photoacoustic imaging; planar measurement geometry; fast algorithm; nonuniform FFT.

AMS Classifications: 35L05, 65R32, 65T50, 92C55.

1 Introduction

Photoacoustic imaging (PAI) is used for visualizing the electromagnetic absorption coefficient of a medium at low frequencies. PAI is based on the physical principle that acoustic waves are excited when a medium is exposed to non-ionizing electromagnetic radiation. The method combines the advantages of optical (high contrast) and ultrasonic imaging and has demonstrated great promise for a variety of biomedical applications, such as imaging of animals [14, 28], early cancer diagnostics [15, 18], and imaging of vasculature [11, 7].

Fourier reconstruction [1, 13, 30] is a well established numerical method for reconstruction of the absorption density when the acoustic signals are recorded with detectors,

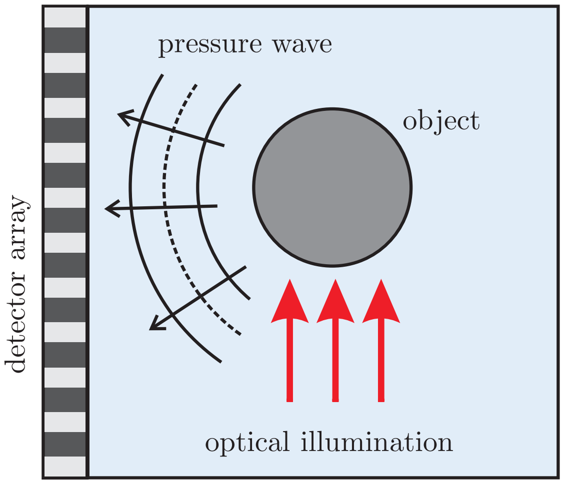

Figure 1: **Setup for photoacoustic imaging.** The object is illuminated with an electromagnetic pulse, which induces an acoustic wave. The acoustic waves are measured with detectors on a plane (or a line).

which are arranged on lines or planes (see Figure 1). These reconstruction techniques can be implemented using the fast Fourier transform (FFT). However, standard FFT algorithm requires sampling on an equally spaced grid, and therefore, in order to implement the reconstruction algorithms interpolation in the Fourier space (see Section 2) is required. Referring to the literature [19] interpolation is a very critical issue, which can lead to sever artifacts (see the examples in Section 5). In this paper, we propose an efficient reconstruction algorithm that uses the nonuniform FFT which provides very accurate reconstructions.

This article is organized as follows: In Section 2 we present the mathematical basics of Fourier reconstruction in PAI. In Section 3 we review the nonuniform FFT which is then used to derive the nonuniform FFT based reconstruction algorithm in Section 4. In Section 5 we present numerical results of the proposed algorithm and compare it with existing Fourier algorithms. The paper concludes with a discussion of some issues related sampling and resolution in Appendix A.

2 Photoacoustic Imaging

Let $C_0^\infty(\mathbb{H})$ denote the space of smooth functions supported in the half space $\mathbb{H} := \mathbb{R}^{d-1} \times (0,\infty)$, $d \geq 2$. Consider the initial value problem

$$\begin{aligned} \left(\partial_t^2 - \triangle\right) p(\mathbf{x},t) &= 0\,, && (\mathbf{x},t) \in \mathbb{R}^d \times (0,\infty)\,, \\ p(\mathbf{x},0) &= f(\mathbf{x})\,, && \mathbf{x} \in \mathbb{R}^d\,, \\ \partial_t p(\mathbf{x},0) &= 0\,, && \mathbf{x} \in \mathbb{R}^d\,, \end{aligned}$$

with $f \in C_0^\infty(\mathbb{H})$. Here $\triangle$ denotes the Laplacian in $\mathbb{R}^d$ and ∂_t is the derivative with respect to t. We write $\mathbf{x} = (x, y)$, $x \in \mathbb{R}^{d-1}$, $y \in \mathbb{R}$, and define the operator $\mathbf{Q} : C_0^\infty(\mathbb{H}) \to C^\infty(\mathbb{R}^d)$ by

$$(\mathbf{Q}\, f)(x, t) := \begin{cases} p(x, y = 0, t)\,, & \text{if } t > 0\,, \\ 0\,, & \text{otherwise}\,. \end{cases}$$

Photoacoustic imaging is concerned with reconstructing $f \in C_0^\infty(\mathbb{H})$ from incomplete and possibly erroneous knowledge of $\mathbf{Q}\, f$. Of particular interest for photoacoustic imaging are the cases $d = 2$ and $d = 3$, see [16, 23, 25, 29].

The operator $\mathbf{Q}$ can be inverted analytically be means of the exact inversion formula

$$(\mathbf{F}_d\, f)(\xi, \eta) = \frac{2\eta\big(\mathbf{F}_d\, \mathbf{Q}\, f\big)\left(\xi, \operatorname{sign}(\eta)\sqrt{|\xi|^2 + \eta^2}\right)}{\operatorname{sign}(\eta)\sqrt{|\xi|^2 + \eta^2}}\,, \qquad (\xi, \eta) \in \mathbb{R}^{d-1} \times \mathbb{R}\,, \tag{1}$$

where the $\mathbf{F}_d$ denotes the d-dimensional Fourier transform,

$$(\mathbf{F}_d\, \varphi)(\boldsymbol{\xi}) := \int_{\mathbb{R}^d} e^{-i\boldsymbol{\xi}\mathbf{x}} \varphi(\mathbf{x})\; d\mathbf{x}\,, \qquad \boldsymbol{\xi} = (\xi, \eta) \in \mathbb{R}^d\,.$$

Equation (1) has been derived in [20, 30] for three spatial dimensions. It can be rigourously proved in any dimension using the inversion formula for the spherical mean Radon transform of [2, 8]. Note that a related formula using the Fourier cosine transform instead of the Fourier transform has been obtained in [12, 13] for $d = 2, 3$.

The inversion formula (1) yields an exact reconstruction, provided that $(\mathbf{Q}\, f)(x, t)$ is given for all $(x, t) \in \mathbb{R}^d$. In practical applications only a *partial* (or *limited view*) data set is available [21, 22, 31]. In this paper we assume that data $(\mathbf{Q}\, f)(x, t)$ are given only for $(x, t) \in (0, X)^d$, see Figure 1, which are modeled by

$$g(x, t) := w_{\text{cut}}(x, t)(\mathbf{Q}\, f)(x, t)\,, \tag{2}$$

where w_{cut} is a smooth nonnegative cutoff function that vanishes outside $(0, X)^d$. Using data (2), the function f cannot be exactly reconstructed in a stable way (see [17, 31]). It is therefore common to apply the exact inverse of $\mathbf{Q}$ to the partial data g and consider the reconstruction as an approximation of the data to be reconstructed. More precisely, the function $f^\dagger$ defined by

$$(\mathbf{F}_d\, f^\dagger)(\xi, \eta) := \frac{2\eta(\mathbf{F}_d\, g)\left(\xi, \operatorname{sign}(\eta)\sqrt{|\xi|^2 + \eta^2}\right)}{\operatorname{sign}(\eta)\sqrt{|\xi|^2 + \eta^2}}\,, \qquad (\xi, \eta) \in \mathbb{R}^d \tag{3}$$

is considered an approximation of f. The function $f^\dagger$ is called *partial reconstruction.*

In this paper we apply the nonuniform FFT to derive a fast algorithm for implementing (3).

3 The Nonuniform Fast Fourier Transform

The discrete Fourier transform of a vector $\mathbf{g} = (g_n)_{n=0}^{N-1} \in \mathbb{C}^N$ with respect to the nodes $\boldsymbol{\omega} = (\omega_k)_{k=-N/2}^{N/2-1}$ (with N even) is defined by

$$T[\mathbf{g}](\omega_k) := \sum_{n=0}^{N-1} e^{-i\omega_k n 2\pi/N} g_n \,, \qquad k = -N/2, \dots, N/2-1 \,. \tag{4}$$

Direct evaluation of the N sums in (4) requires $\mathcal{O}(N^2)$ operations. Using the classical fast Fourier transform (FFT) this effort can be reduced to $\mathcal{O}(N \log N)$ operations. However, application of the classical FFT is restricted to the case of equispaced nodes $\omega_k = k$, $k = -N/2, \dots, N/2-1$.

The nonuniform FFT (see [3, 6, 9, 24, 26]) is an approximate but highly accurate method for evaluating (4) at arbitrary nodes ω_k, $k = -N/2, \dots, N/2-1$ in $\mathcal{O}(N \log N)$ operations.

To derive the nonuniform FFT we closely follow the presentation of [9], which is based on the following lemma:

Lemma 3.1 ([9, Proposition 1]). *Let $c > 1$ and $\alpha < \pi(2c-1)$. Assume that $\Psi : \mathbb{R} \to \mathbb{R}$ is continuous in $[-\alpha, \alpha]$, vanishing outside $[-\alpha, \alpha]$, and positive in $[-\pi, \pi]$. Then*

$$e^{-i\omega\theta} = \frac{c}{2\pi\Psi(\theta)} \sum_{j\in\mathbb{Z}} \hat{\Psi}(\omega - j/c) e^{-ij\theta/c} \,, \qquad \omega \in \mathbb{R} \,, |\theta| \le \pi \,. \tag{5}$$

Here $\hat{\Psi}(\omega) := \int_{\mathbb{R}} e^{-i\omega\theta}\Psi(\theta) d\theta$ denotes the one dimensional Fourier transform of Ψ.

Proposition 3.2. *Let c, α, Ψ, and $\hat{\Psi}$ be as in Lemma 3.1. Then, for every $\mathbf{g} = (g_n)_{n=0}^{N-1} \in \mathbb{C}^N$ and $\omega \in \mathbb{R}$ we have*

$$\sum_{n=0}^{N-1} e^{-i\omega n 2\pi/N} g_n = \sum_{j\in\mathbb{Z}} e^{-i\pi(\omega - j/c)} \hat{\Psi}(\omega - j/c) \hat{G}_j \,, \tag{6}$$

with

$$\hat{G}_j := \frac{c}{2\pi} \left(\sum_{n=0}^{N-1} \frac{g_n e^{-ijn2\pi/(Nc)}}{\Psi(n2\pi/N - \pi)} \right) , \qquad j \in \mathbb{Z} \,. \tag{7}$$

Proof. Taking $\theta = n2\pi/N - \pi \in [-\pi, \pi]$ in (5), gives

$$e^{-i\omega n 2\pi/N} = \frac{c}{2\pi\Psi(n2\pi/N - \pi)} \sum_{j\in\mathbb{Z}} \hat{\Psi}(\omega - j/c) e^{-ijn2\pi/N} e^{-i\pi(\omega - j/c)} \,,$$

and therefore

$$\sum_{n=0}^{N-1} e^{-i\omega n 2\pi/N} g_n = \frac{c}{2\pi} \sum_{n=0}^{N-1} \sum_{j\in\mathbb{Z}} e^{-i\pi(\omega - j/c)} \hat{\Psi}(\omega - j/c) \frac{g_n e^{-ijn2\pi/(Nc)}}{\Psi(n2\pi/N - \pi)} \,.$$

Interchanging the order of summation in the right hand side of the above equation shows (6), (7) and concludes the proof. $\square$

In the following we assume that cN is an even number. Then

$$\hat{G}_j = \frac{c}{2\pi} \left(\sum_{n=0}^{cN-1} \frac{g_n}{\Psi(n2\pi/N - \pi)} e^{-ijn2\pi/(Nc)} \right) , \qquad j \in \mathbb{Z} , \tag{8}$$

where $g_n := 0$ for $n \geq N$, is an oversampled discrete Fourier transform with the oversampling factor c. Moreover we assume that $\hat{\Psi}$ is concentrated around zero and decays rapidly away from zero. The nonuniform FFT uses the formulas (6), (8) to evaluate $T[g]$ at the nodes ω_k. The basic steps of the algorithm are as follows:

(i) Append $(c-1)N$ zeros to the vector $\mathbf{g} = (g_n)_{n=0}^{N-1}$ and evaluate $\hat{G}_j$, $j = -Nc/2, \ldots, Nc/2-1$, in (8) with the FFT algorithm.

(ii) Evaluate the sums in (6) approximately by using only the terms with $|\omega_k - j/c| \leq K$, where the *interpolation length* K is a small positive parameter.

Since $\hat{\Psi}$ is assumed to decay rapidly, the truncation error in Step (ii) is small.

The nonuniform Fourier transform is summarized in Algorithm 1:

Algorithm 1 Nonuniform FFT with respect to the nodes $\boldsymbol{\omega} = (\omega_k)_{k=-N/2}^{N/2-1}$, using input vector $\mathbf{g} = (g_n)_{n=0}^{N-1}$, oversampling $c > 1$, interpolation length K, and window width $\pi < \alpha < \pi(2c-1)$.

```
$\mathbf{\Psi} \leftarrow \big(\Psi(2\pi n/N - \pi)\big)_n$                                   ▷ precomputations
$\hat{\mathbf{\Psi}} \leftarrow \big(e^{-i(\omega_k - j/c)\pi/c}\hat{\Psi}(\omega_k - j/c)\big)_{k,j}$

function nufft($\mathbf{g}, \boldsymbol{\omega}, c, K, \mathbf{\Psi}, \hat{\mathbf{\Psi}}$)
    $\mathbf{g} \leftarrow \mathbf{g}/\mathbf{\Psi} \cdot c/(2\pi)$
    $\mathbf{g} \leftarrow \big(\mathbf{g}, \mathtt{zeros}(1, (c-1)N\big)$                   ▷ zero-padding
    $\mathbf{g} \leftarrow \mathtt{fft}(\mathbf{g})$                                     ▷ one dimensional FFT
    for $k = -N/2, \ldots, N/2-1$ do
        $\hat{g}_k \leftarrow \sum_{|j - c\omega_k| \leq cK} \hat{\Psi}_{k,j} g_j$              ▷ truncated summation of (6)
    end for
    return $(\hat{g}_k)_k$
end function
```

In Algorithm 1 all evaluations of Ψ and $\hat{\psi}$ are precomputed and stored. Moreover the classical FFT is applied to a vector of length cN. Therefore the numerical complexity of Algorithm 1 is $\mathcal{O}(cN \log N)$. Typically $c = 2$, in which case the numerical effort of the nonuniform FFT is essentially twice the effort of the one dimensional classical FFT applied to an input vector of the same length. See [9, Section 3] for an exact operation count, and a comparison between actual computation times of the classical and the nonuniform FFT.

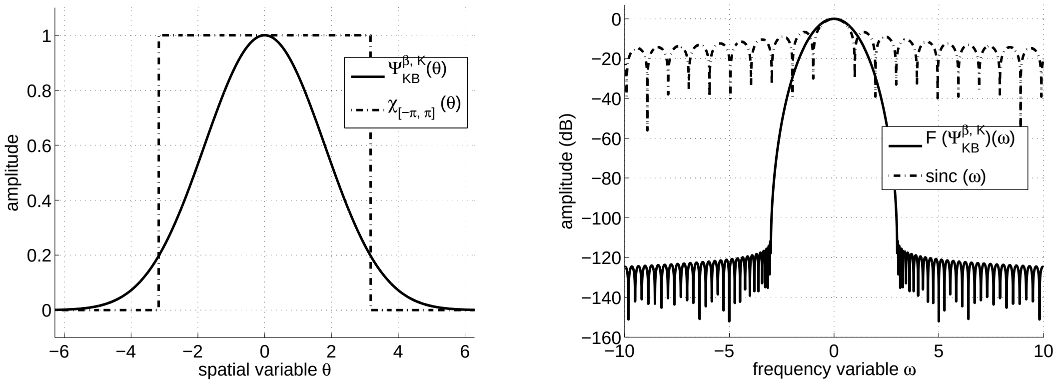

Figure 2: *Left:* Kaiser-Bessel window $\Psi_{\text{KB}}^{\alpha,K}(\theta)$ and characteristic function of the interval $[-\pi,\pi]$. *Right:* Fourier transforms $\hat{\Psi}_{\text{KB}}^{\alpha,K}(\omega)$ and $2\pi\,\text{sinc}(\omega)$ in dB (decibel). Here dB denotes the logarithmic decay $10\log_{10}(\phi(\omega)/\phi(0))$ of some quantity $\phi(\omega)$.

In our implementation we choose for Ψ the *Kaiser Bessel window*,

$$\Psi_{\text{KB}}^{\alpha,K}(\theta) := \frac{1}{I_0(\alpha K)}\begin{cases} I_0(K\sqrt{\alpha^2-\theta^2})\,, & \text{if } |\theta| \le \alpha\,, \\ 0\,, & \text{if } |\theta| > \alpha\,. \end{cases}$$

Here I_0 is the modified Bessel function of order zero. The one dimensional Fourier transform of $\Psi_{\text{KB}}^{\alpha,K}$ is

$$\hat{\Psi}_{\text{KB}}^{\alpha,K}(\omega) = \begin{cases} 2\sinh(\alpha\sqrt{K^2-\omega^2})/\big(I_0(\alpha K)\sqrt{K^2-\omega^2}\big), & \text{if } \omega \in \mathbb{R}\setminus\{-K,K\}\,, \\ 2\alpha/(I_0(\alpha K)), & \text{otherwise}\,. \end{cases}$$

The Kaiser Bessel window is a good and often used candidate for Ψ, since $\hat{\Psi}_{\text{KB}}^{\alpha,K}(\omega)$ becomes extremely small for $|\omega| > K$. Exemplarily, for the parameters $K = 3$, and $\alpha = 3\pi$, we have

$$\frac{\hat{\Psi}_{\text{KB}}^{\alpha,K}(K)}{\hat{\Psi}_{\text{KB}}^{\alpha,K}(0)} = \frac{\alpha K}{\sinh(\alpha K)} \simeq 3 * 10^{-11}\,,$$

see Figure 2.

Remark 3.3. *Take* $c = 1$ *and let* Ψ *be the characteristic function of the interval* $[-\pi,\pi]$. *Then* $\hat{\Psi}(\omega) = 2\pi\,\text{sinc}(\pi\omega)$ *and (6), (7) reduce to the sinc series*

$$\sum_{n=0}^{N-1} e^{-i\omega n 2\pi/N} g_n = \sum_{j\in\mathbb{Z}} e^{-i\pi(\omega-j)}\,\text{sinc}(\omega-j)\left(\sum_{n=0}^{N-1} g_n e^{-ijn2\pi/N}\right)\,,$$

which is a discretized version of Shannon's sampling formula [19, 27]

$$\hat{g}(\omega) = \sum_{j\in\mathbb{Z}} e^{-i\pi(\omega-j)}\,\text{sinc}(\omega-j)\hat{g}(j)$$

applied to the Fourier transform of a function g *supported in* $[0,2\pi]$.

See Figure 2 for a comparison of sinc *and* $\hat{\Psi}_{\mathrm{KB}}^{\alpha,K}$*, with* $K = 3$ *and* $\alpha = 3\pi$*. One realizes that* $\hat{\Psi}_{\mathrm{KB}}^{\alpha,K}$ *decays much faster than* sinc *and is therefore much better suited for truncated interpolation. In fact,* $\hat{\Psi}_{\mathrm{KB}}^{\alpha,K}(\omega)$ *is in the order of double precision for* $|\omega| > 3$*, whereas* $|\operatorname{sinc}(\omega)| < 0.01$ *only for* $\omega > 100/\pi$*.*

An error estimate for the nonuniform FFT using the Kaiser Bessel window is given in [9]. The result is

$$\left| e^{-i\omega\theta} - \frac{c}{2\pi\Psi(\theta)} \sum_{|\omega - j/c| < K} \hat{\Psi}_{\mathrm{KB}}^{\alpha,K}(\omega - j/c) e^{-ij\theta/c} \right| \le \frac{30}{\pi I_0(K/c^2\pi\sqrt{\alpha^2 - 1})} .$$

Exemplarily, taking $c = 2$, $\alpha = 3\pi$ and $K = 3$, the above error is as small as $3 * 10^{-8}$.

4 A Fourier Reconstruction Algorithm based on the Nonuniform FFT

In this section we apply the nonuniform FFT to photoacoustic imaging. Throughout the following we restrict our attention to two dimensions, noting that the general case $d \ge 2$ can be treated in an analogous manner.

Assume that $f \in C_0^\infty\big((0, X)^2\big)$, and set $g := w_{\mathrm{cut}}\, \mathbf{Q} f$, where w_{cut} is as in (2). Fourier reconstruction names an implementation of (3), that uses discrete data

$$g_{m,n} := g(m\Delta_{\mathrm{samp}}, n\Delta_{\mathrm{samp}}) , \qquad (m, n) \in \{0, \dots, N - 1\}^2 , \tag{9}$$

and reconstructs an approximation

$$f_{m,n} \simeq f^\dagger(m\Delta_{\mathrm{samp}}, n\Delta_{\mathrm{samp}}) , \qquad (m, n) \in \{0, \dots, N - 1\}^2 . \tag{10}$$

Here $f^\dagger$ is defined by (3), N is an even number and $\Delta_{\mathrm{samp}} := X/N$. In appendix Appendix A we show that the sampling in (10), (9) is sufficiently fine, provided that $\Delta_{\mathrm{samp}} \le \pi/\Omega$, where Ω is the essential bandwidth of f.

Discretizing (3) with the trapezoidal rule gives

$$\sum_{n=0}^{N-1} \left(\sum_{m=0}^{N-1} e^{-i(ln+km)2\pi/N} f_{m,n} \right) = \frac{2k}{\omega_{k,l}} \sum_{n=0}^{N-1} e^{-i\omega_{k,l} n 2\pi/N} \left(\sum_{m=0}^{N-1} e^{-ikm2\pi/N} g_{m,n} \right) , \tag{11}$$

where

$$\omega_{k,l} := \operatorname{sign}(l) \sqrt{k^2 + l^2} , \qquad (k, l) \in \{-N/2, \dots, N/2 - 1\}^2 .$$

Now one notices that the inner sums in (11),

$$\tilde{g}_{k,n} := \sum_{m=0}^{N-1} e^{-ikm2\pi/N} g_{m,n} , \qquad (k, n) \in \{-N/2, \dots, N/2 - 1\} \times \{0, \dots, N - 1\} , \tag{12}$$

can be evaluated with N one dimensional FFTs, and the outer sums

$$\hat{g}_{k,l} := \sum_{n=0}^{N-1} e^{-i\omega_{k,l} n 2\pi/N} \tilde{g}_{k,n}\,, \qquad (k,l) \in \{-N/2, \dots, N/2-1\}^2\,, \tag{13}$$

with N nonuniform FFTs. Having evaluated $\hat{g}_k(\omega_{k,l})$ we set $\hat{f}_{k,l} := \frac{2k\,\hat{g}_{k,l}}{\omega_{k,l}}$ and finally find

$$f_{n,m} := \frac{1}{N^2} \sum_{k,l=N/2}^{N/2-1} e^{i(km+ln)2\pi/N} \hat{f}_{k,l}\,, \qquad (m,n) \in \{0, \dots, N-1\}^2\,, \tag{14}$$

with the two dimensional FFT.

Algorithm 2 Nonuniform FFT based algorithm for calculating $\mathbf{f} = (f_{m,n})_{n,m=0}^{N-1}$ using data $\mathbf{g} = (g_{m,n})_{m,n=0}^{N-1}$, oversampling factor c, interpolation length K, and window size $\pi < \alpha < \pi(2c-1)$.

```
function FouRecNufft($\mathbf{g}, \alpha, c, K$)
    for $n = 0, \dots, N-1$ do
        $\mathbf{h} \leftarrow (g_{m,n})_m$
        $(\tilde{g}_{k,n})_k \leftarrow \texttt{fft}(\mathbf{h})$                      ▷ one dimensional FFT
    end for
    $\mathbf{l} \leftarrow (-N/2, \dots, N/2-1)$
    for $k = -N/2, \dots, N/2-1$ do
        $\boldsymbol{\omega} \leftarrow \texttt{sign}(\mathbf{l})\sqrt{k^2 + \mathbf{l}^2}$
        $\mathbf{h} \leftarrow \texttt{nufft}(\mathbf{g}, \boldsymbol{\omega}, c, K, \boldsymbol{\Psi}, \hat{\boldsymbol{\Psi}})$   ▷ nonuniform FFT, Algorithm 1
        $(f_{k,l})_l \leftarrow k\,\mathbf{h}/\boldsymbol{\omega}$
    end for
    $\mathbf{f} \leftarrow (f_{k,l})_{k,l}$
    $\mathbf{f} \leftarrow \texttt{ifft2}(\mathbf{f})$                          ▷ two dimensional inverse FFT
    return $\mathbf{f}$
end function
```

The nonuniform FFT based reconstruction algorithm is summarized in Algorithm 2. Its numerical complexity can easily be estimated. Evaluating (12) requires $N\mathcal{O}(N \log N)$ operations (N one dimensional FFTs), evaluating (13) requires $N\mathcal{O}(N \log N)$ operations (N non-uniform FFTs), and (14) is evaluated with the inverse two dimensional FFT in $\mathcal{O}(N^2 \log N)$ operations. Therefore the overall complexity of Algorithm 1 is $\mathcal{O}(N^2 \log N)$.

In the following we compare the numerical performance of Algorithm 2 with the standard Fourier algorithms presented in the literature [10, 30], which all differ in the way how the sums in (13) are evaluated:

1. **Direct Fourier reconstruction.** Equation (13) cannot be evaluated with the classical FFT algorithm because the nodes $\omega_{k,l}$ are non-equispaced. The most simple way to evaluate (13) is with direct summation. Because there are N^2 such sums in (13), direct Fourier reconstruction requires $\mathcal{O}(N^3)$ operations. Consequently it does

not lead to a fast algorithm. However, since (13) is evaluated exactly, it is optimally suited to evaluate reconstructions of fast Fourier algorithms.

2. **Linear interpolation based reconstruction.** A fast and simple alternative to direct Fourier reconstruction is as follows: Choose an oversampling factor $c \geq 1$ and evaluate
$$\hat{g}_k(\omega) := \Delta_{\mathrm{samp}} \sum_{n=0}^{N-1} e^{-i\omega n 2\pi/N} \tilde{g}_{k,n} \,,$$
at the uniformly spaced nodes $\omega = \Delta_{\mathrm{samp}} j/c$, $j \in \{0, \dots, Nc-1\}$ exactly. In a next step, linear interpolation is used to find approximate values $\hat{g}_{k,l} \simeq \hat{g}_k(\omega_{k,l})$.

3. **Truncated** sinc **reconstruction.** If the function Ψ in Algorithm 2 is chosen as the characteristic function of the interval $[-c\pi, c\pi]$, $c \geq 1$, then the nonuniform fast Fourier transform reduces to the truncated sinc interpolation considered in [10]. However, due to the slow decay of $\mathrm{sinc}(\omega)$, truncation will introduce a non-negligible error in the reconstructed image (see Remark 3.3).

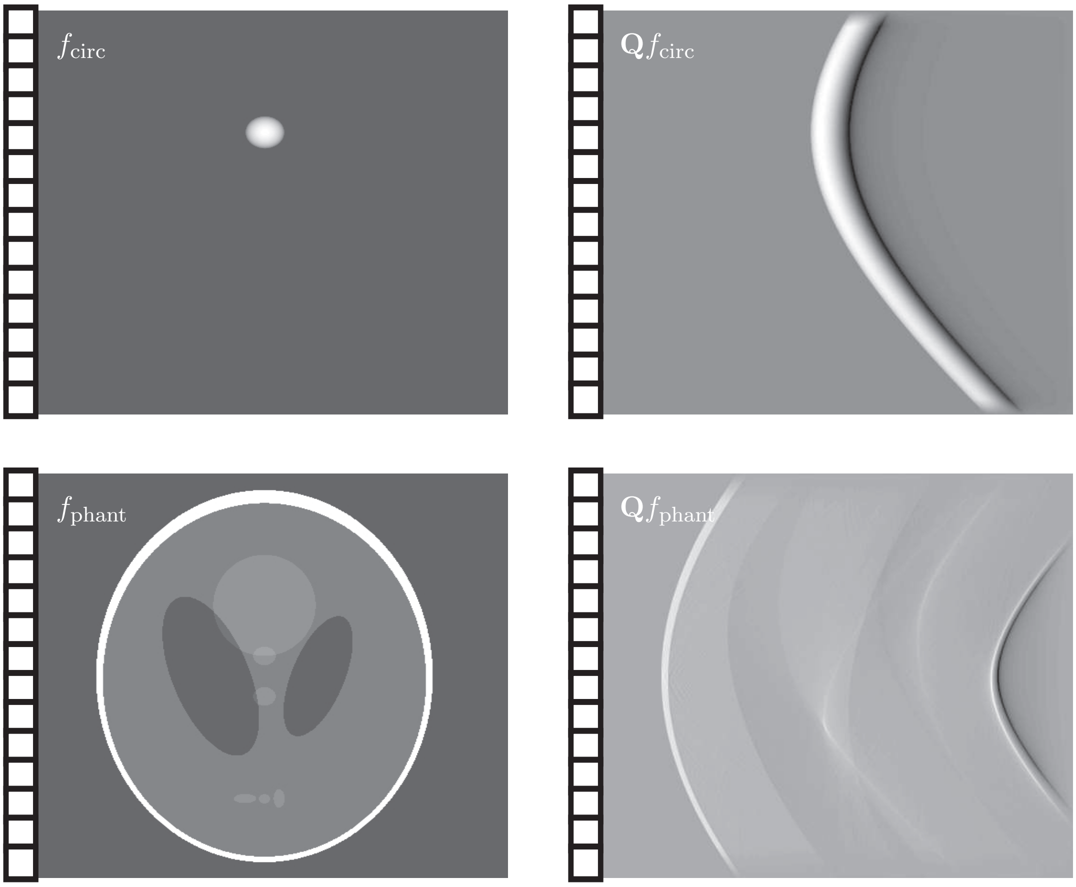

Figure 3: Phantoms and corresponding data used in the numerical test.

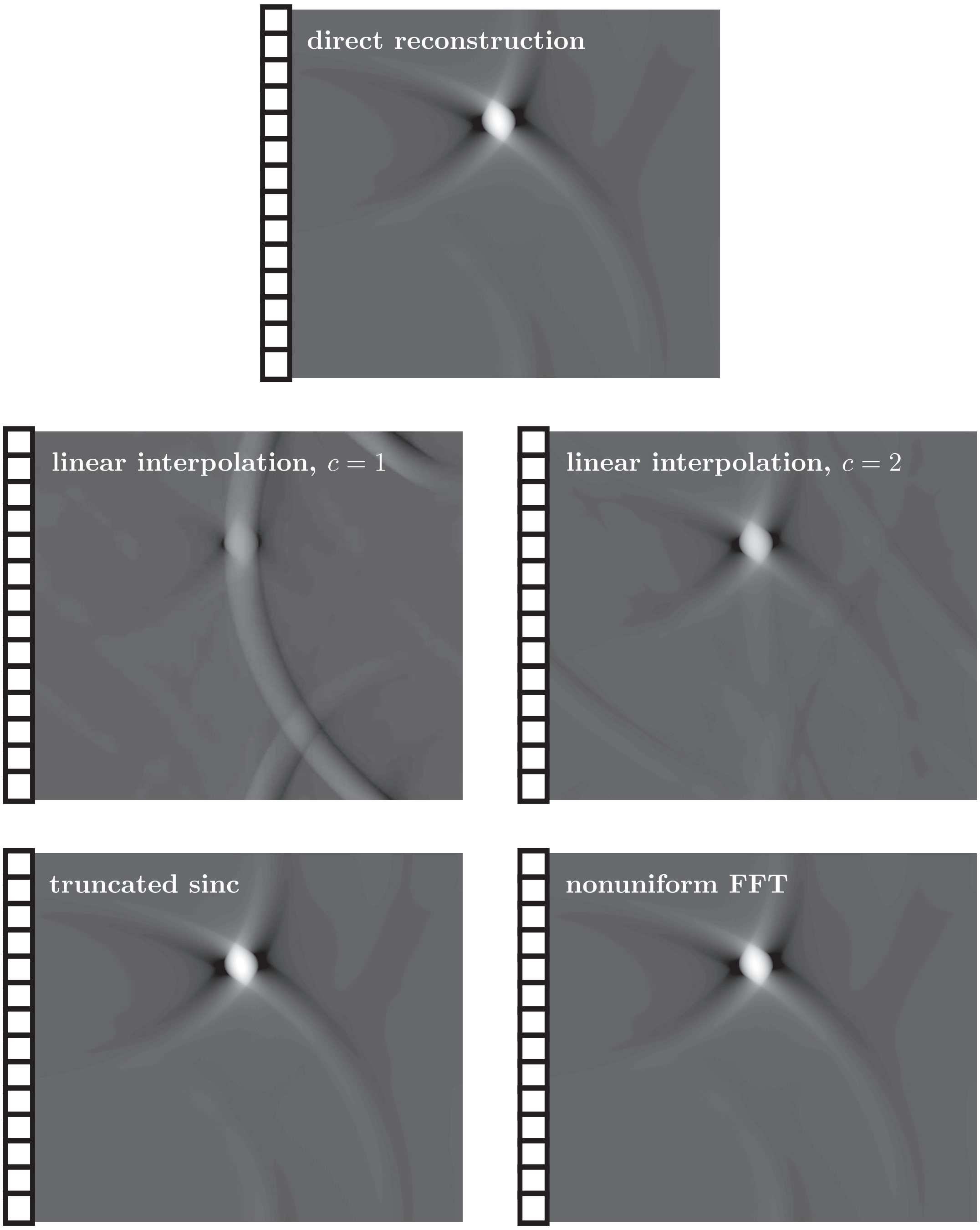

Figure 4: Reconstruction of f_{circ}. White corresponds to function value 1, black to function value -0.4. *Top Line:* Direct Fourier reconstruction. *Middle line:* Linear interpolation based reconstruction without (left) and with (right) oversampling. *Bottom line:* Truncated sinc (left) and nonuniform FFT based reconstruction (right).

5 Numerical Examples

In the following we numerically evaluate nonuniform FFT based, truncated sinc, linear interpolation based, and direct Fourier reconstruction. In all numerical experiments we use $N = 512$, $X = 1$. For the nonuniform FFT and the truncated sinc interpolation we

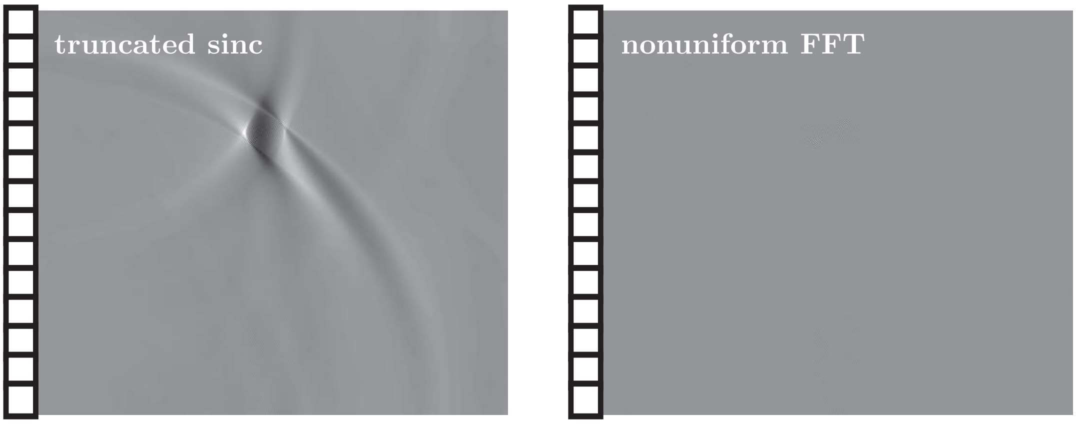

Figure 5: Differences between and direct and truncated sinc reconstruction (left), and direct and nonuniform FFT based reconstruction (right). White (resp. black) corresponds to function value 0.05 (resp. -0.05).

choose the oversampling factor $c = 2$, interpolation length $K = 3$, and window width $\alpha = 3\pi - 0.02$.

The cutoff function $w_{\rm cut}$ is constructed by convolution of

$$\varphi_\epsilon(x,t) = \begin{cases} C_\epsilon \exp\bigl(-1/(\epsilon - x^2 - t^2)^4\bigr), & \text{if } x^2 + t^2 < \epsilon\,, \\ 0, & \text{otherwise}\ , \end{cases}$$

with the characteristic function of $[0,1]^2$, where ϵ is a small parameter and C_ϵ is chosen in such a way that $\int_{\mathbb{R}^2} \varphi_\epsilon(x,t)dxdt = 1$. Typically, ϵ is chosen as a "small" multiple of the sampling step size $\Delta_{\rm samp} = 1/N$.

1. As first case example we use a circular shaped object

   $$f_{\rm circ}(x) = \begin{cases} \bigl(a^2 - |\mathbf{x} - \mathbf{x}_0|^2\bigr)^{1/2}, & \text{if } |\mathbf{x} - \mathbf{x}_0| < a\,, \\ 0, & \text{otherwise}\,, \end{cases}$$

   centered at $\mathbf{x}_0 := (x_0, y_0)$, see Figure 3. For such a simple object reconstruction artifacts can be identified very clearly. Moreover, the data $\mathbf{Q}\, f_{\rm circ}$ can be evaluated analytically (see [4, Equation (B.1)]) as

   $$(\mathbf{Q}\, f_{\rm circ})(x,0,t) = \operatorname{Re}\left[(s_+ - s_-) - t \log\left(\frac{s_+ + (t + a_i)}{s_- + (t - a_i)}\right)\right]\ .$$

   Here $s_\pm := ((t \pm a)^2 + |(x,0) - \mathbf{x}_0|^2)^{1/2}$, $\log(\cdot)$ is the principal branch of the complex logarithm, and $\operatorname{Re}[z]$ denotes the real part of complex number z. The reconstruction results are depicted in Figures 4 and 5.

2. In the next example we consider the Shepp–Logan phantom $f_{\rm phant}$, which is shown in bottom right image in Figure 3. The data were calculated numerically by imple-

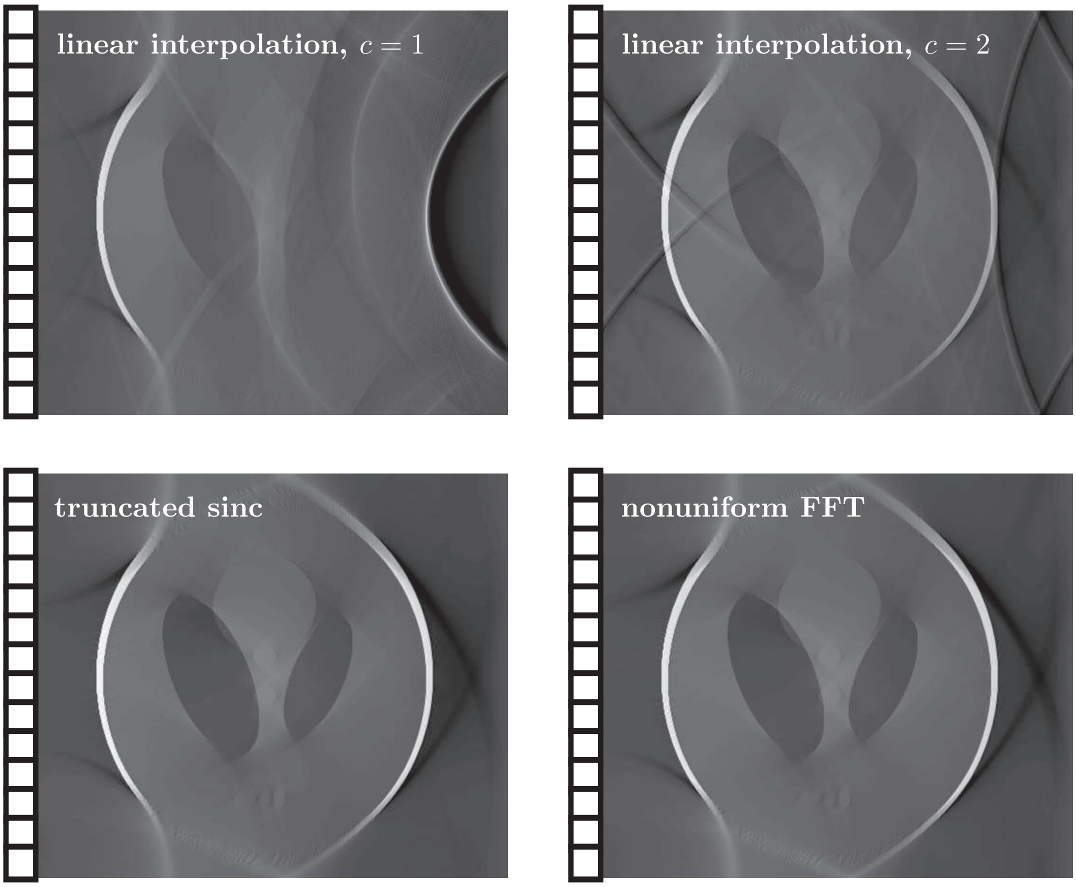

Figure 6: Reconstructions of f_{phant}. *Top line:* Linear interpolation based reconstruction without (left) and with (right) oversampling. *Bottom line:* Reconstructions using truncated sinc (left) nonuniform FFT based reconstruction (right).

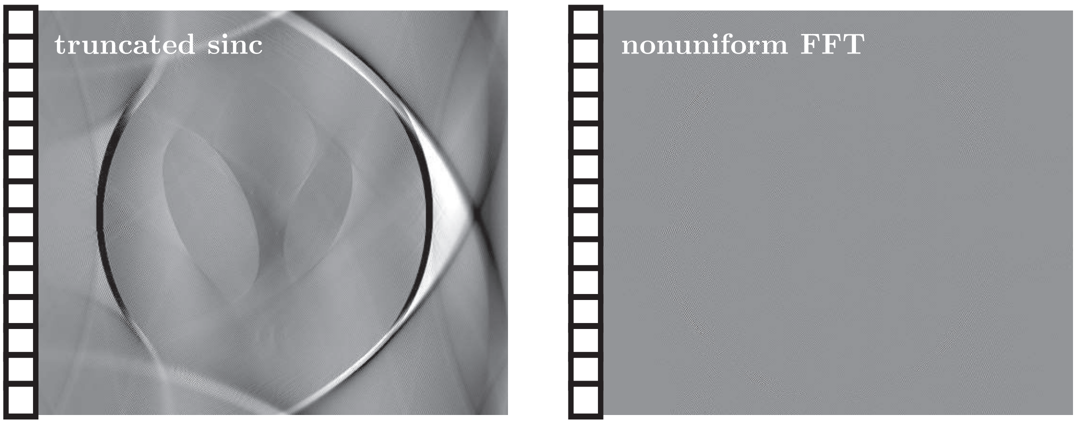

Figure 7: Differences between and direct and truncated sinc reconstruction (left), and direct and nonuniform FFT based reconstruction (right). White (resp. black) corresponds to function value 0.05 (resp. -0.05)

menting d'Alemberts formula [5],

$$(\mathbf{Q}\, f_{\text{phant}})(x, 0, t) = \int_0^t \frac{r(\partial_r\, \mathbf{M}\, f_{\text{phant}})(x, 0, r)}{\sqrt{t^2 - r^2}}\; dr$$

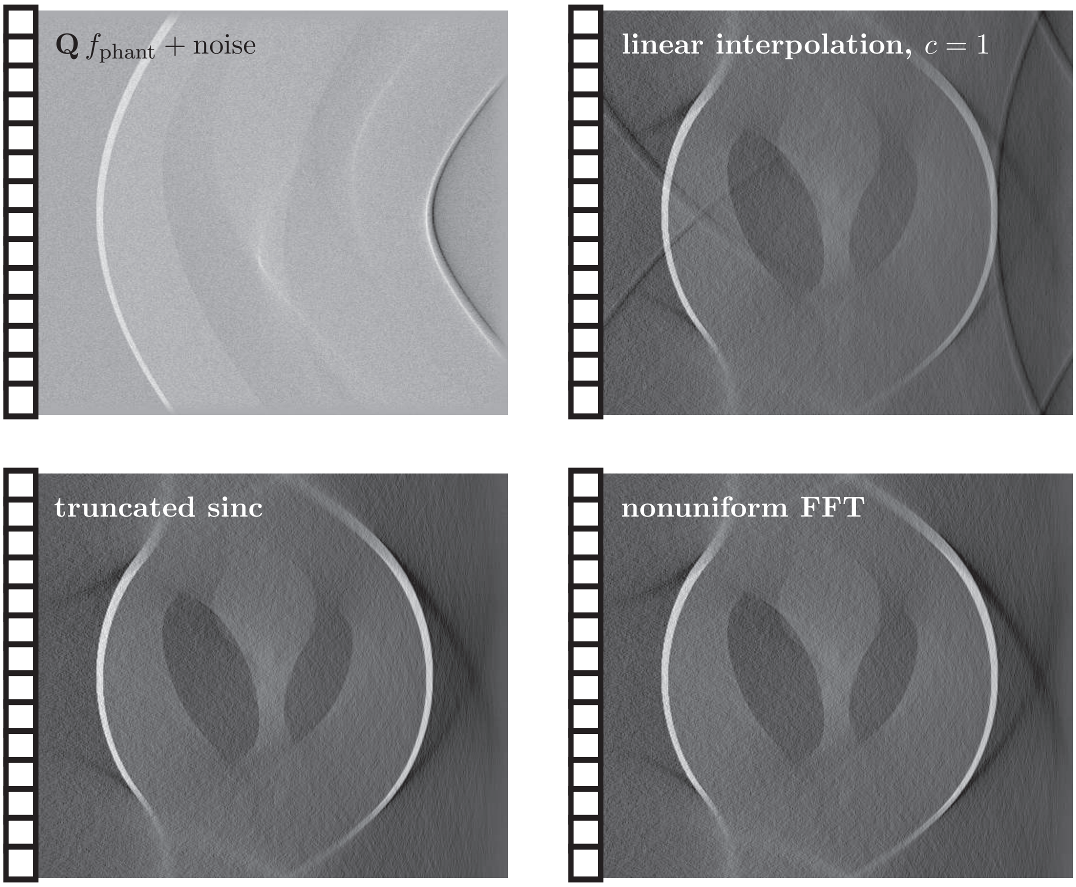

Figure 8: Reconstruction of f_{phant} from noisy data. *Top line:* Noisy data (left) and reconstruction using linear interpolation (right). *Bottom line:* Truncated sinc (left) and nonuniform FFT based reconstruction (right).

with

$$(\mathbf{M}\, f_{\text{phant}})(x,0,t) := \frac{1}{2\pi} \int_{S^1} f_{\text{phant}}\big((x,0) + t\omega\big) d\omega$$

denoting the *spherical mean transform.* The reconstruction results from simulated data are depicted in Figures 6 and 7.

In order to demonstrate the stability of the Fourier algorithms, we also performed reconstructions from noisy data, where Gaussian noise was added with a variance equal to 10% of the maximal data value. The reconstruction results are depicted in Figure 8.

Discussion

We emphasize that none of the above discussed algorithms has been designed to calculate an approximation of f but an approximation of to the partial reconstruction $f^\dagger$ defined in (3). Therefore even in the direct reconstruction (top left image in Figure 4) one can see some blurred boundaries appear in the reconstructed images. Such artifacts are expected using limited view data (2), see [17, 31]

The results of linear interpolation based reconstruction without oversampling ($c = 1$) are quite useless. The reconstructions can be significantly improved by using a larger oversampling factor c. However, even then, the results never reach the quality of the nonuniform FFT based reconstruction. Moreover, the numerical effort of linear interpolation based reconstruction is proportional to the oversampling factor, which prohibits the use of "very large" values for c. In the reconstruction with $c = 2$ (middle line in Figure 4 and top line in Figure 6) artifacts are still clearly visible.

The images in the bottom lines of Figures 4 and 6 suggest that truncated sinc and nonuniform FFT based reconstruction seem to perform quite similar. However the differences to the direct Fourier reconstructions in Figure 5 and 7 demonstrate the higher accuracy of the nonuniform FFT based algorithm.

6 Conclusion

We presented a novel fast Fourier reconstruction algorithm for photoacoustic imaging using a limited detector array. The proposed algorithm is based on the nonuniform FFT. Theoretical investigation as well as numerical simulations show that our algorithm produces better images than existing Fourier algorithms with the same numerical complexity. Moreover the proposed algorithm is insensitive against noise.

Acknowledgement

This work has been supported by the Austrian Science Foundation (FWF) within the framework of the NFN "Photoacoustic Imaging in Biology and Medicine", Project S10505-N20. Moreover, the work of M. Haltmeier has been supported by the Technology transfer office of the University Innsbruck (transIT).

A Sampling and Resolution

Let $f \in C_0^\infty\big((0, X)^d\big)$ and define g, $f^\dagger$ by (2), (3). We further assume that $\mathbf{F}_d\, w_{\mathrm{cut}}$ is centered around zero and that f is essentially bandlimited with essential bandwidth Ω, in the sense that $(\mathbf{F}_d\, f)(\boldsymbol{\xi})$ is negligible for $|\boldsymbol{\xi}| \geq \Omega$. Note that since f has bounded support, $\mathbf{F}_d\, f$ cannot vanish exactly on $\{|\boldsymbol{\xi}| \geq \Omega\}$.

- **Sampling of g.** Equation (1) implies that

$$(\mathbf{F}_d\, g)(\xi, \omega) = (\mathbf{F}_d\, w_{\mathrm{cut}}) * (\mathbf{F}_d\, \mathbf{Q}\, f)\,(\xi, \omega)\,, \qquad (\xi, \omega) \in \mathbb{R}^d\,, \tag{15}$$

with

$$(\mathbf{F}_d\, \mathbf{Q}\, f)(\xi, \omega) = \begin{cases} \frac{2\omega (\mathbf{F}_d\, f)\left(\xi, \mathrm{sign}(\omega)\sqrt{\omega^2 - |\xi|^2}\right)}{\mathrm{sign}(\omega)\sqrt{\omega^2 - |\xi|^2}}\,, & \text{if } |\omega| > |\xi|^2\,, \\ 0\,, & \text{otherwise}\,. \end{cases}$$

The assumption that f has essential bandwidth Ω and equation (15) imply that $(\mathbf{F}_d\, g)(\xi, \omega)$ is negligible outside the set

$$K := \{(\xi, \omega) : |\xi| \leq |\omega| \leq \Omega\} \subset (-\Omega, \Omega)^d \,.$$

Now Shannon's sampling theorem [19, 27] states that g is sufficiently fine sampled if the step size in x and in t satisfies the Nyquist condition $\Delta_{\text{samp}} = \pi/\Omega$.

- **Sampling of $f^\dagger$.** Similar considerations as above again show that $f^\dagger$ is essentially bandlimited with essential bandwidth Ω. Shannon's sampling theorem implies that $f^\dagger$ can be reliable reconstructed from discrete samples taken with step size $\Delta_{\text{samp}} = \pi/\Omega$.

If f has essential bandwidth larger than Ω, the function g has to be filtered with a low pass-filter *before* sampling. Otherwise, sampling introduces aliasing artifacts in the reconstructed image [19].

Theoretically the resolution (at least of the visible parts) can be increased ad infinity by simply decreasing the sampling size Δ_{samp}. In practical applications several other factors (such as the bandwidth of the ultrasound detection system) limit the bandwidth of the data [29]. This also guarantees that in practise a moderate sampling step size Δ_{samp} gives correct sampling without aliasing.

References

[1] M. A. Anastasio, D. Zhang, J. Modgil, and P. L. La Riviere. Application of inverse source concepts to photoacoustic tomography. *Inverse Problems*, 23:S21–S35, 2007.

[2] L.-E. Andersson. On the determination of a function from spherical averages. *SIAM Journal on Mathematical Analysis*, 19:214–232, 1988.

[3] G. Beylkin. On the fast Fourier transform of functions with singularities. *Applied and Computational Harmonic Analysis*, 2, 1995.

[4] P. Burgholzer, J. Bauer-Marschallinger, H. Grün, M. Haltmeier, and G. Paltauf. Temporal back-projection algorithms for photoacoustic tomography with integrating line detectors. *Inverse Problems*, 23:S65–S80, 2007.

[5] R. Courant and D. Hilbert. *Methods of Mathematical Physics*, volume 2. Wiley-Interscience, New York, 1962.

[6] A. Dutt and V. Rokhlin. Fast Fourier transforms for nonequispaced data. *SIAM Journal on Scientific Computing*, 14(6), 1993.

[7] R. O. Esenaliev, I. V. Larina, K. V. Larin, D. J. Deyo, M. Motamedi, and D. S. Prough. Optoacoustic technique for noninvasive monitoring of blood oxygenation: a feasibility study. *Applied Optics*, 41:4722–4731, 2002.

[8] J. A. Fawcett. Inversion of n-dimensional spherical averages. *SIAM Journal on Applied Mathematics*, 45:336–341, 1985.

[9] K. Fourmont. Non-equispaced fast Fourier transforms with applications to tomography. *Journal of Fourier Analysis and Applications*, 9(5):431–450, 2003.

[10] M. Jaeger, S. Schüpbach, A. Gertsch, M. Kitz, and M. Frenz. Fourier reconstruction in optoacoustic imaging using truncated regularized inverse k-space interpolation. *Inverse Problems*, 23:S51–S63, 2007.

[11] R. G. M. Kolkman, E. Hondebrink, W. Steenbergen, and F. F. M De Mul. In vivo photoacoustic imaging of blood vessels using an extreme-narrow aperture sensor. *IEEE Journal of Selected Topics in Quantum Electronics*, 9:343–346, 2003.

[12] K. P. Köstli and P. C. Beard. Two-dimensional photoacoustic imaging by use of fourier-transform image reconstruction and a detector with an anisotropic response. *Applied Optics*, 42, 2003.

[13] K. P. Köstli, M. Frenz, H. Bebie, and H. P. Weber. Temporal backward projection of optoacoustic pressure transients using fourier transform methods. *Physics in Medicine and Biology*, 46:1863–1872, 2001.

[14] R. A Kruger, W. L. Kiser, D. R. Reinecke, G. A. Kruger, and K. D. Miller. Thermoacoustic molecular imaging of small animals. *Molecular Imaging*, 2:113–123, 2003.

[15] R. A. Kruger, K. D. Miller, H. E. Reynolds, W. L. Kiser, D. R. Reinecke, and G. A. Kruger. Breast cancer in vivo: contrast enhancement with thermoacoustic ct at 434 mhz-feasibility study. *Radiology*, 216:279–283, 2000.

[16] P. Kuchment and L. A. Kunyansky. Mathematics of thermoacoustic tomography. *European Journal Applied Mathematics*, 19:191–224, 2008.

[17] A. K. Louis and E. T. Quinto. Local tomographic methods in sonar. In *Surveys on solution methods for inverse problems*, pages 147–154. Springer, Vienna, 2000.

[18] S. Manohar, A. Kharine, J. C. G. van Hespen, W. Steenbergen, and T. G. van Leeuwen. The twente photoacoustic mammoscope: system overview and performance. *Physics in Medicine and Biology*, 50:2543–2557, 2005.

[19] F. Natterer and F. Wübbeling. *Mathematical Methods in Image Reconstruction.* SIAM, Philadelphia, 2001.

[20] S. J. Norton and M. Linzer. Ultrasonic reflectivity imaging in three dimensions: Exact inverse scattering solutions for plane, cylindrical and spherical apertures. *IEEE Transactions on Biomedical Engineering*, 28:2002–2020, 1981.

[21] G. Paltauf, R. Nuster, M. Haltmeier, and P. Burgholzer. Experimental evaluation of reconstruction algorithms for limited view photoacoustic tomography with line detectors. *Inverse Problems*, 23:S81–S94, 2007.

[22] X. Pan and M. A. Anastasio. On a limited-view reconstruction problem in diffraction tomography. *IEEE Transactions on Medical Imaging*, 21:413–416, 2002.

[23] S. K. Patch and O. Scherzer. Special section on photo- and thermoacoustic imaging. *Inverse Problems*, 23:S1–S122, 2007.

[24] D. Potts, G. Steidl, and M. Tasche. Fast Fourier transforms for nonequispaced data: a tutorial. In *Modern sampling theory*, Applied Numerical Harmonic Analysis, pages 247–270. Birkhäuser Boston, 2001.

[25] O. Scherzer, M. Grasmair, H. Grossauer, M. Haltmeier, and F. Lenzen. *Variational Methods in Imaging*. Springer, 2008. to appear.

[26] G. Steidl. A note on fast Fourier transforms for nonequispaced grids. *Advances in Computational Mathematics*, 9(3-4):337–352, 1998.

[27] M. Unser. Sampling—50 Years after Shannon. *Proceedings of the IEEE*, 88(4):569–587, 2000.

[28] X. D. Wang, G. Pang, Y. J. Ku, X. Y. Xie, G. Stoica, and L. V. Wang. Noninvasive laser-induced photoacoustic tomography for structural and functional in vivo imaging of the brain. *Nature Biotechnology*, 21:803–806, 2003.

[29] M. Xu and L. V. Wang. Photoacoustic imaging in biomedicine. *Review of Scientific Instruments*, 77:041101, 2006.

[30] Y. Xu, D. Feng, and L. V. Wang. Exact frequency–domain reconstrcution for thermoacosutic tomography — i: Planar geometry. *IEEE Transactions on Medical Imaging*, 21:823–828, 2002.

[31] Y. Xu, L. V. Wang, G. Ambartsoumian, and P. Kuchment. Reconstructions in limited-view thermoacoustic tomography. *Medical Physics*, 31:724–733, 2004.